CHAPTER 4

Illustration of monovalent and polyvalent ion storage in vanadyl acetate

Illustration of monovalent and polyvalent ion storage in vanadyl acetate

4.1 Introduction

Vanadyl acetate [$VO(CH_3COO)_2$] is a vanadium containing one dimensional organic-inorganic material. The crystal structure is made up of interconnected VO_6 octahedra and two acetate ions [1, 2]. Wen et al. showed the possibility of Zn^{2+} ion and Li^+ ion storage in vanadyl acetate [3, 4]. However, to the best of our knowledge, there is a lack of systematic study on vanadyl acetate for electrochemical capacitor. Therefore, we examined the electrochemical storage behavior of vanadyl acetate with respect to Na^+, Mg^{2+} and Al^{3+} ions in aqueous electrolytes. It is quite intriguing to reveal that vanadyl acetate exhibits contrasting storage behaviors in these electrolytes. It was found that it is electrochemically more stable with Na^+ ion rather than Mg^{2+} and Al^{3+} ions. It is also illustrated that silica based gel electrolyte helped in further improving the long term stability for Na^+ ion storage.

4.2 Experimental Section

4.2.1 Materials

Ammonium metavanadate (NH_4VO_3), Carbon black and N-methyl-2-pyrrolidone were procured from (Alfa Aesar). Acetic acid glacial (99-100 %), Nitic Acid, Sodium chloride, Sodium sulfate anhydrous, Magnesium Chloride, Magnesium sulfate, Aluminium chloride anhydrous powder, Aluminuim sulphate 16-hydrate, Aluminium nitrate monohydrate and Sulfuric acid were collected from (Merck). Polyvinyl alcohol (PVA) (M_w ~ 125,000) and Polyvinylidene fluoride (PVDF) were obtained from (Sigma Aldrich), Graphite powder (Lobachemie Pvt. Ltd), MWCNT (Sisco Research laboratory, SRL), Ammonia solution (NH_4OH, Rankem, Avantor Performance Materials India Ltd.), Aerosil 200 (fumed silica gel, SRL), Xanthum gum powder (Fssai, nuage India), Ethanol and Distilled water.

4.2.2 Synthesis

4.2.2.1 *Synthesis of vanadyl acetate*

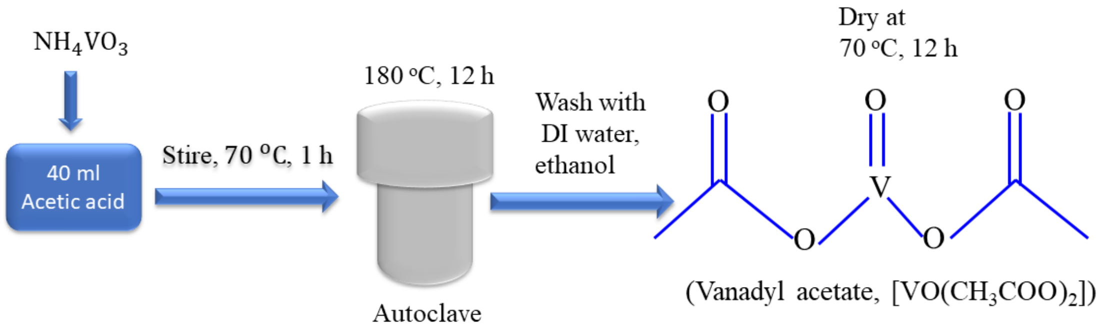

Figure 4.1: Schematic diagram of synthesis of vanadyl acetate.

As shown in the above schematic diagram (Figure 4.1), vanadyl acetate ([$VO(CH_3COO)_2$], abbreviated as VA) was synthesized by a facile hydrothermal method reported in the literature [3, 4]. Typically, 10 mmol ammonium metavandate (NH_4VO_3) was mixed with 40 ml of acetic acid (glacial) by stirring for 1 h at 70 ^{0}C to get homogeneous reddish brown solution. Then the solution was transferred to a 50 ml stainless steel autoclave and maintained at 180 °C for 24 h. After cooling down to room temperature, the obtained green precipitate was washed with distilled water and ethanol for several times and finally dried at 70 °C overnight.

4.2.3 Characterization

The structural characteristics of the prepared materials were examined by powder X ray diffraction (P-XRD, BRUER AXS D8 FOCUS, Cu-K_α radiation; λ = 1.5406Å) and Raman spectroscopy (RENISHAW BASIS SERIES WITH 515 LASER, RENISHAW, UK). Field emission scanning electron microscope (FESEM, JEOL, JSM – 7200F) was used to examine the surface morphology. A thermogravimetric analyzer (TGA) was used to conduct the thermal analysis.

4.2.4 Electrochemical Analysis

The electrode slurry was formed by mixing the active material, carbon black and PVDF binder in the weight ratio of 8:1:1 in the solvent of N-methyl-2-pyrrolidone (NMP). Then it was drop coated on graphite foil and finally dried in oven at temperature of 90 °C for overnight. The weight of active material on each electrode varies from 1 mg to 1.2 mg. The electrochemical experiments were performed out in

Metrohm Autolab (PGSTAT302N) using three electrode system with Ag/AgCl as reference electrode, Platinum electrode as counter electrode and VA as working electrode and the used electrolytes were 0.5 M Na_2SO_4, 1 M NaCl, 1 M $MgSO_4$, 1 M $MgCl_2$, 0.5 M $Al_2(SO_4)_3$ and 1 M $AlCl_3$. For symmetric electrochemical capacitor experiments, two electrode system is employed with both the electrodes as VA // VA. A mass balance was maintained while evaluating the symmetric electrochemical capacitor. The utilized aqueous and gel electrolytes are named as 0.5 M Na_2SO_4 (aq), 0.5 M Na_2SO_4/Gum (gel) and 0.5 M Na_2SO_4/Silica (gel). 0.5 M Na_2SO_4/Gum (gel) and 0.5 M Na_2SO_4/Silica (gel) electrolytes were prepared by mixing separately 5 wt% xanthum gum powder and 8 wt% silica foam to 0.5 M Na_2SO_4 aqueous solution. The digital photograph for both the gel electrolytes are given in the Figure 4.2. The specific capacitance for three electrode and two electrode system were calculated by the equation (4.1) and (4.2) respectively.

$$C_s = \frac{I\Delta t}{m\Delta V} \ (Fg^{-1}) \ldots\ldots\ldots\ldots\ldots\ldots (4.1)$$

$$C_{cell} = \frac{2I\Delta t}{m\Delta V} \ (Fg^{-1}) \ldots\ldots\ldots\ldots\ldots.. (4.2)$$

where I represent the applied current (A), Δt represent the discharge time (s), m represent the active mass on the electrode (g) and ΔV represent the discharge potential interval (V).

Moreover, the energy density (E) and power density (P) were estimated by equations (4.3) and (4.4) respectively.

$$E = \frac{1}{2} C_{cell} (\Delta V)^2 \times \frac{1000}{3600} \ \text{Wh kg}^{-1} \ldots\ldots\ldots\ldots\ldots.. (4.3)$$

$$P = \frac{I\Delta V}{2m} \times 1000 \ \text{W kg}^{-1} \ldots\ldots\ldots\ldots\ldots\ldots\ldots\ldots (4.4)$$

where, the symbols signify their usual meanings as mentioned above [5, 6].

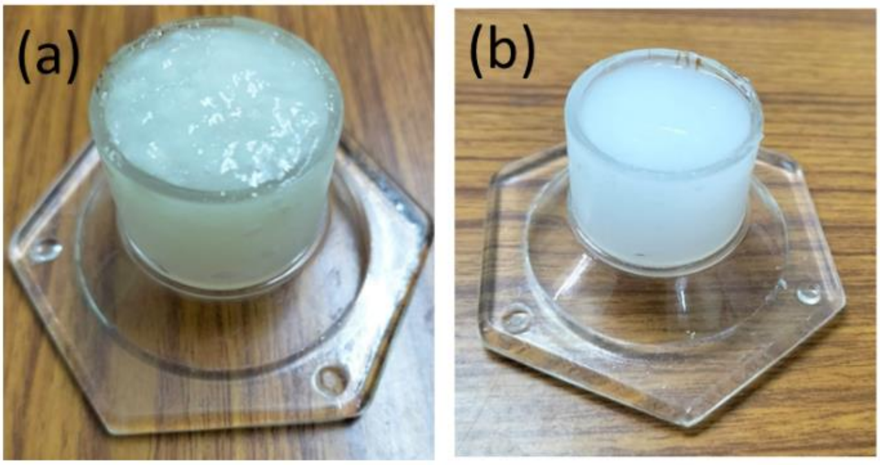

Figure 4.2: Digital photographs of (a) 0.5 M Na_2SO_4/Gum (gel) and (b) 0.5 M Na_2SO_4/Silica (gel) electrolytes.

4.3 Results and discussion

Figure 4.3a shows the XRD pattern of the VA, where all the diffraction peaks are indexed with orthorhombic lattice (PDF# 50-0572). Figure 4.3b depicts the thermogravimetric analysis of VA, in which the slight weight loss at 54 ^oC indicates the evaporation of solvents such as ethanol, water etc. The decomposition of VA occurs around 200 ^oC which is due to the breaking of acetic acid and formation of vanadium pentoxide (V_2O_5) [3, 4]. Figure 4.3c shows the Raman analysis of VA, in which the intense peak at 150 cm^{-1}, corresponds to the chain translation associated to the layered structure. The peaks recognized at 265 cm^{-1}, and 695 cm^{-1} indicate the H-O bond. Apart from that, the peaks centered at 429 cm^{-1} and 524 cm^{-1} are interconnected with V-O-V stretching vibration [4, 7, 8]. Another peak marked at 989 cm^{-1} is correlated with the V=O stretching mode [4, 7, 8]. FESEM image (Figure 4.3d) indicates nanobelt like structure of VA.

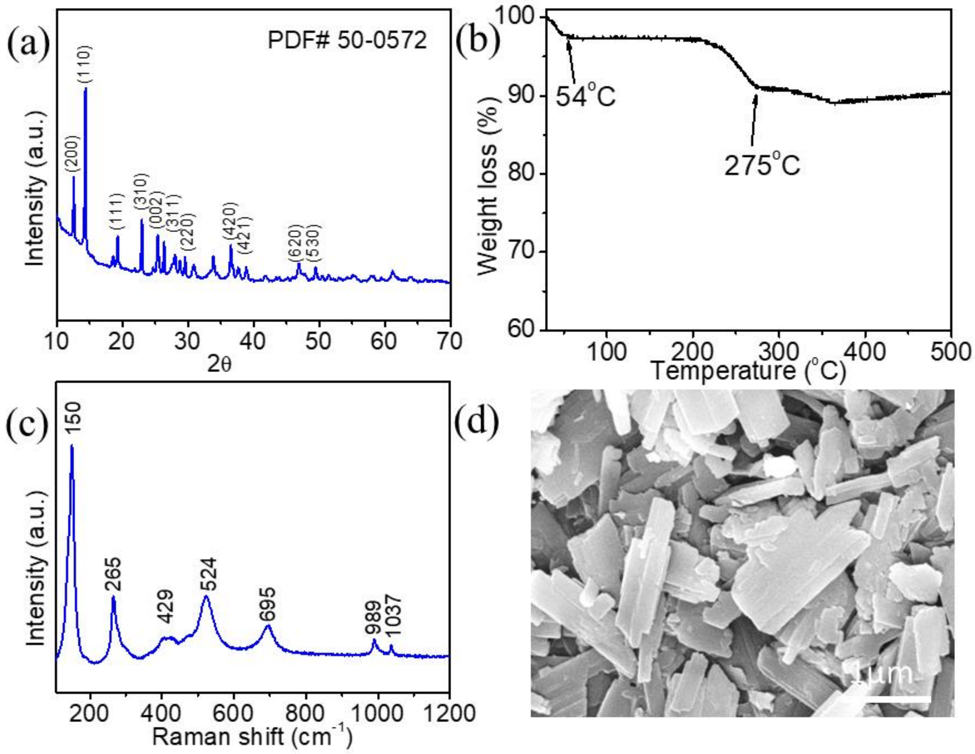

Figure 4.3: (a) XRD pattern, (b) Raman spectrum, (c) TGA and (d) FESEM image of VA.

In order to study the electrochemical activity, initially cyclic voltammetry (CV) experiments of VA were performed in 0.5 M $Al_2(SO_4)_3$ and 1 M $AlCl_3$ electrolytes in the potential window -0.8 V to 0.5 V (V vs Ag/AgCl) at the scan rate of 2 mVs^{-1}. As shown in the (Figure 4.4a), the cathodic peaks are observed at (-0.01 V) and (-0.26 V) in the case of 0.5 M $Al_2(SO_4)_3$, while anodic peaks are at (0.13 V) and (0.33 V). Almost similar behavior is seen for 1 M $AlCl_3$ aqueous electrolyte (Figure 4.4b).

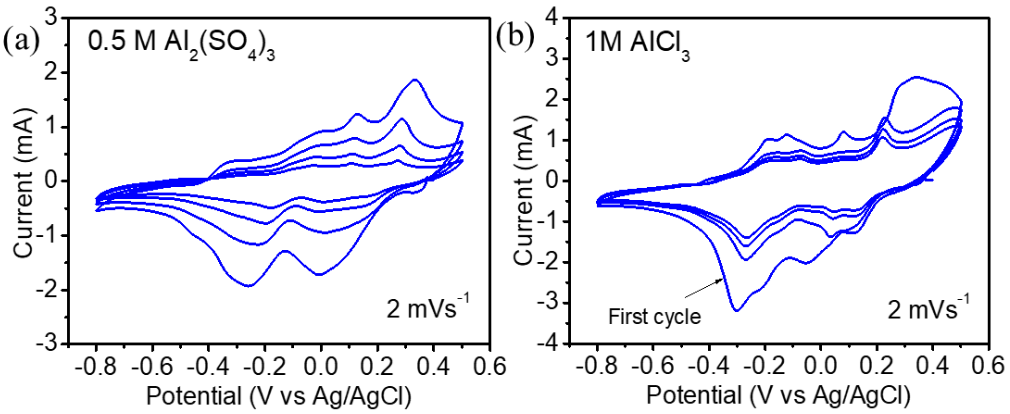

Figure 4.4: CV profiles of VA in (a) 0.5 M $Al_2(SO_4)_3$ and (b) 1 M $AlCl_3$ at a scan rate of 2 mVs^{-1}.

CV experiments were also performed in 1 M NaCl and 1 M LiCl aqueous electrolytes (Figure 4.5a and 4.5b), in the similar potential window and scan rate, where it could be seen that the CV curves are quite different when compared with aqueous 0.5 M $Al_2(SO_4)_3$ and 1 M $AlCl_3$ electrolytes (Figure 4.4a and 4.4b). Therefore, it indirectly suggests the influence of Al^{3+} ion in VA. Moreover, to examine any proton storage in VA, CV experiments were conducted in 1 M HCl, 1 M H_2SO_4 and DI water in the similar potential window and no noticeable redox peaks could be observed (Figure 4.6 (a-c)).

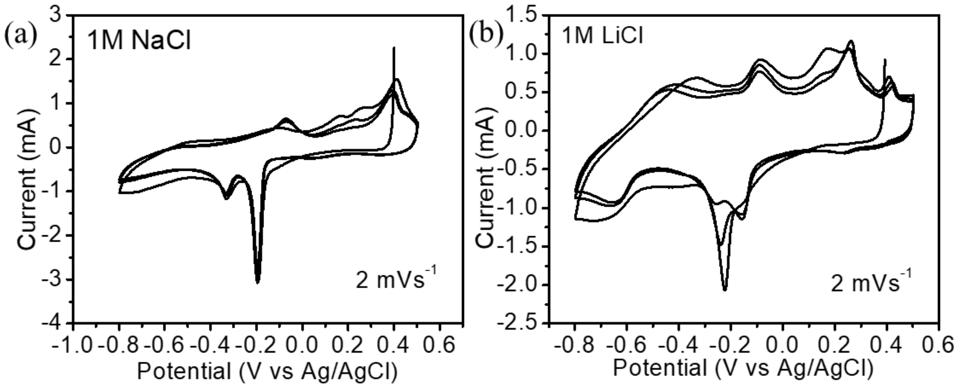

Figure 4.5: CV profiles of VA in (a) 1 M NaCl and (b) 1 M LiCl aqueous electrolytes.

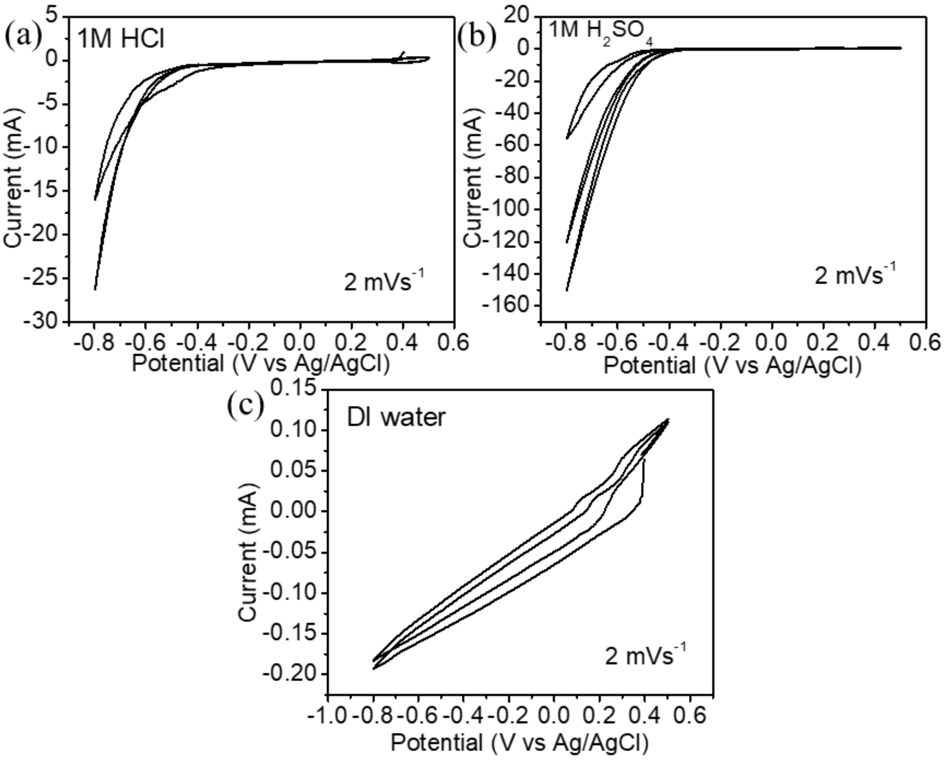

Figure 4.6: CV profiles of VA in (a) 1 M HCl and (b) 1 M H_2SO_4 aqueous electrolytes and (c) DI water.

Now to evaluate the Al^{3+} ion storage capacity in VA, galvanostatic charge discharge (GCD) experiments were conducted in the same potential window (i.e. -0.8 to 0.5 V) for the aqueous 0.5 M $Al_2(SO_4)_3$ and 1 M $AlCl_3$ electrolytes at current density 1 Ag^{-1} (Figure 4.7 (a-b)). There are no prominent discharge and charge potential plateaus for 0.5 M $Al_2(SO_4)_3$ aqueous electrolyte. However, they are mostly contributing in the range of -0.4 to 0.2 V which is consistent with CV profiles. The initial discharge and charge specific capacitances were found to be 732 Fg^{-1} and 350 Fg^{-1} respectively (Figure 4.7a). Similar behavior was also observed for 1 M $AlCl_3$ aqueous electrolyte. This again validated the CV profiles. The specific capacitances during the first cycle were calculated to be 543 Fg^{-1} and 440 Fg^{-1} for the discharge and charge states respectively (Figure 4.7b).

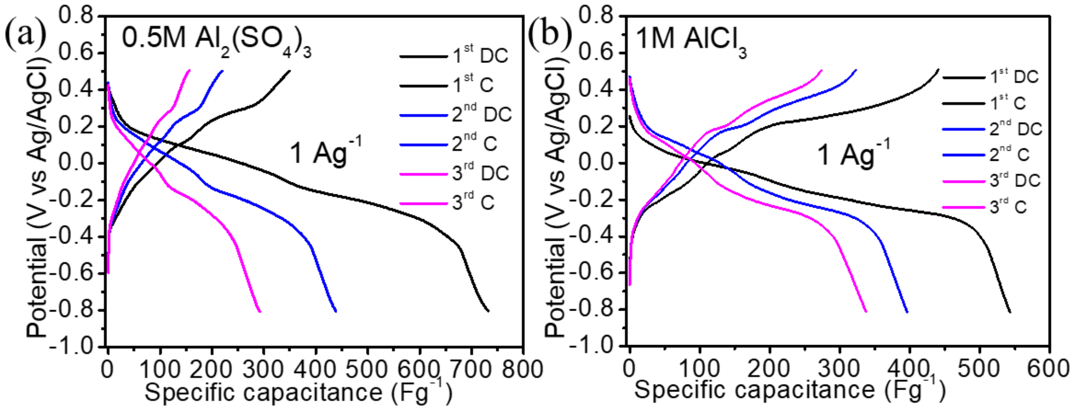

Figure 4.7: Discharge-charge profiles of VA in (a) 0.5 M $Al_2(SO_4)_3$ and (a) 1 M $AlCl_3$ aqueous electrolytes.

Then we conducted the GCD experiments for cycling stability test. Figure 4.8 shows the comparison of long cycle stabilities up to 100 cycles, where, highly capacity fading observed during the initial cycles for both electrolytes (0.5 M $Al_2(SO_4)_3$ and 1 M $AlCl_3$. However, the obtained specific capacitance values after 100 cycles were found as 30 Fg^{-1} and 39 Fg^{-1}.

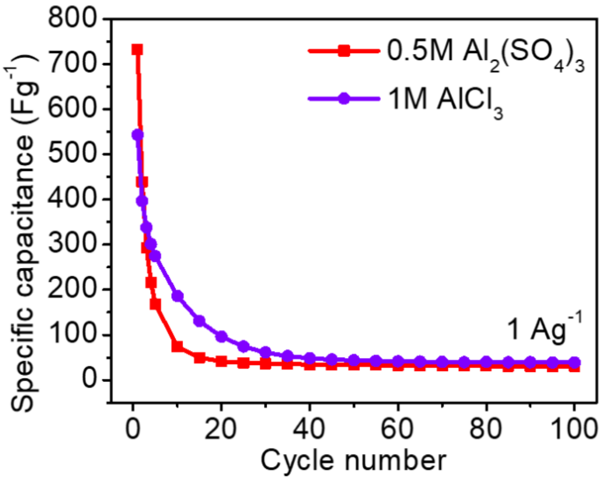

Figure 4.8: Comparison of long cycle stability of VA in 0.5 M $Al_2(SO_4)_3$ and 1 M $AlCl_3$ aqueous electrolytes at current density of 1 Ag^{-1}.

It was reported in some literatures about the improvement of cycle stability by increasing the pH of the electrolyte as well as utilizing gel electrolytes [9, 10]. Therefore, we increased the pH of 1 M $AlCl_3$ electrolyte to 3.6 by adding a small amount NH_4OH and termed as 1 M $AlCl_3/NH_4OH$ (aq, pH=3.6). Besides, the gel electrolyte was prepared by adding 8 wt % of polyvinyl alcohol (PVA) in 1 M $AlCl_3$ solution and later added NH_4OH till precipitation. The pH of the gel electrolyte was 3.4 and the electrolyte is termed as 1 M $AlCl_3/NH_4OH$/PVA (gel, pH=3.4). Figure (4.9a and 4.9b) show the CV profiles of VA at scan rate of 2 mVs^{-1} in 1 M $AlCl_3/NH_4OH$ (aq, pH=3.6) and 1 M $AlCl_3/NH_4OH$/PVA (gel, pH=3.4) electrolytes, which exhibits similar electrochemical behaviors. From the charge-discharge profiles, the initial discharge and charge specific capacitances of VA for 1 M $AlCl_3/NH_4OH$ (aq, pH=3.6) electrolyte were found to be 852 Fg^{-1} and 434 Fg^{-1} respectively (Figure 4.9c). In contrast, discharge and charge specific capacitances of VA for the first cycles were estimated as 1351 Fg^{-1} and 486 Fg^{-1} respectively for the case of 1 M $AlCl_3/NH_4OH$/PVA (gel, pH=3.4) electrolyte (Figure 4.9d). These values are quite high as compared to pristine 1 M $AlCl_3$ electrolyte. Although capacity decline is noticed, the stable specific capacitance values of 72 Fg^{-1} and 80 Fg^{-1} over 100 cycles at current density of 1 Ag^{-1} are estimated for 1 M $AlCl_3/NH_4OH$ (aq, pH=3.6) and 1 M $AlCl_3/NH_4OH$/PVA (gel, pH=3.4) electrolytes respectively (Figure 4.9e). There is a minor improvement in stability in both the cases as compared to pristine 1 M $AlCl_3$. The reason due to this improvement can be stated as: increase in pH value of aqueous electrolyte and using the gel electrolyte may lead to the decrease in electrode degradation [9].

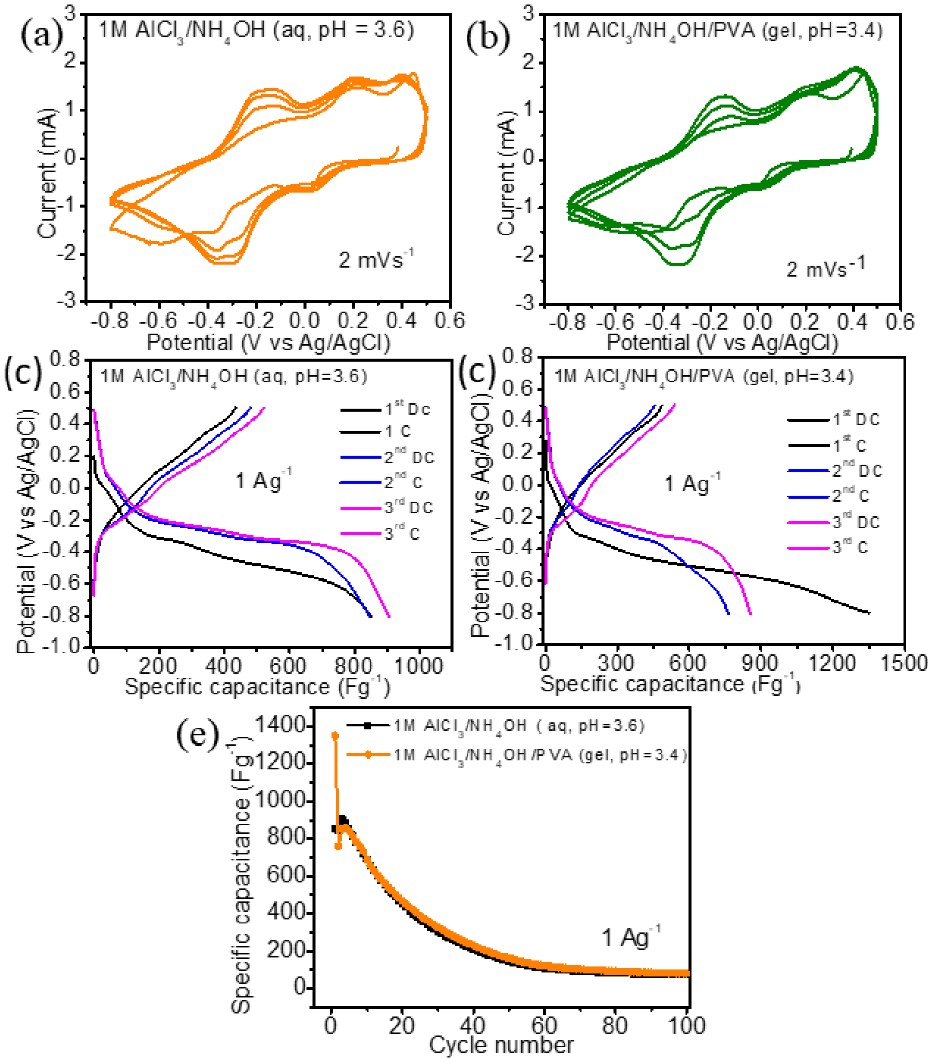

Figure 4.9: CV profiles of VA (a) 1 M $AlCl_3/NH_4OH$ (aq, pH=3.6) and (b) 1 M $AlCl_3/NH_4OH$/PVA (gel, pH=3.4) electrolytes, Discharge-charge profiles of VA in (c) 1 M $AlCl_3/NH_4OH$ (aq, pH=3.6) and (d) 1 M $AlCl_3/NH_4OH$/PVA (gel, pH=3.4) electrolytes and (e) Comparison of cycle stabilities.

Overall, since the capacity fading is occurring in all the cases and the cycling stability could not significantly enhance, therefore, we planned to incorporate some conducting materials such as reduced graphene oxide (rGO) and carbon nanotube (CNT) in pristine VA material. The materials were synthesized following synthesize procedure of VA. About 15 mg of rGO or CNT was dispersed in the acetic acid solution. Rest of the synthesis parameters were kept constant and the obtained materials were termed as rGO/VA and CNT/VA. Figure 4.10a shows the XRD patterns of rGO/VA and CNT/VA, where all the diffraction peaks were matched pristine VA. For the further confirmation, Raman analysis also performed for rGO/VA and CNT/VA and noticed similar Raman characteristic peaks as VA (Figure 4.10b). But additional two Raman peaks centered at 1362 cm^{-1} and 1581 cm^{-1} for rGO/VA could be recognized as D and G bang of rGO respectively (inset view of Figure 4.10b) [11]. Similarly, the D and G band of CNT were marked at 1358 cm^{-1} and 1586 cm^{-1} in the case CNT/VA composite (inset view of Figure 4.10b) [12]. Apart from that, the surface morphology analysis also conducted through FESEM process. Figure (4.11a and 4.11b) depicts FESEM images of pure rGO and CNT respectively. Figure 4.11c shows a FESEM image of rGO/VA in a nanobelt configuration, with the rGO sheet clearly visible. Figure 4.11d depicts the FESEM image of CNT/VA, in which a similar morphology was detected with the extra image of CNT.

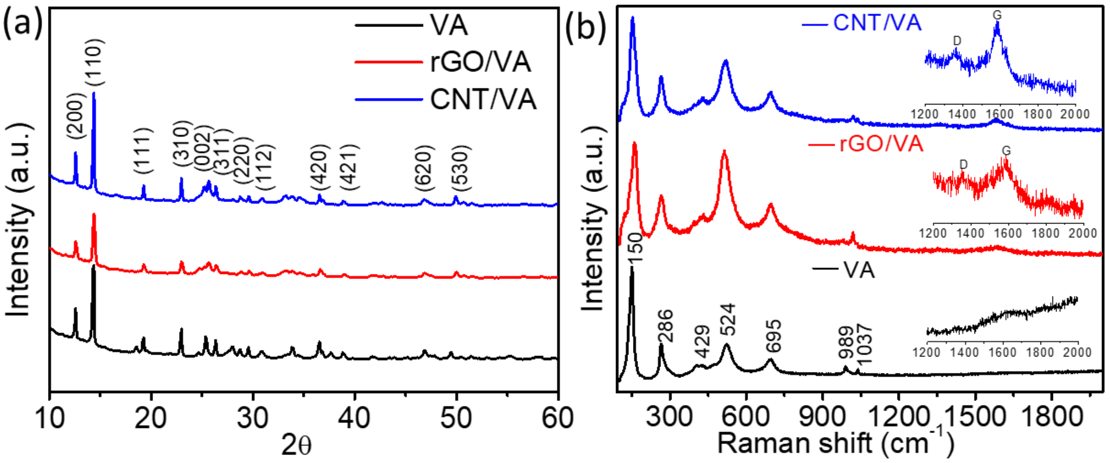

Figure 4.10: (a) XRD and (b) Raman spectrum of VA, rGO/VA and CNT/VA.

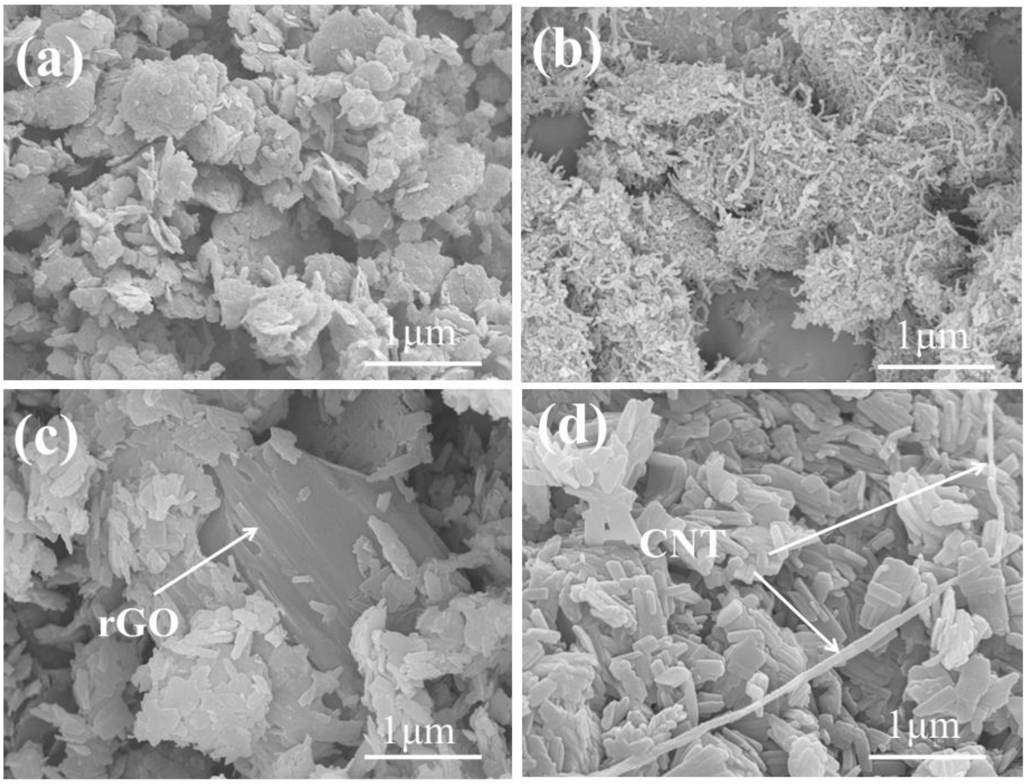

Figure 4.11: FESEM images of (a) rGO, (b) CNT, (c) rGO/VA and (d) CNT/VA.

Now, to investigate the electrochemical activity and charge storage capacity, CV and GCD experiments were performed for both rGO/VA as well as CNT/VA. Figure (4.12a and 4.12b) shows the CV profiles of rGO/VA and CNT/VA in 1 M $AlCl_3$ aqueous electrolyte at a scan rate of 2 mVs^{-1} respectively. It was observed that the electrochemical behaviors of rGO/VA and CNT/VA are almost same with VA except the slight change in the redox peak positions. For a comparison, galvanostatic charge-discharge experiments were performed for rGO/VA and CNT/VA in 1 M $AlCl_3$ aqueous electrolyte at the current density of 1 Ag^{-1} (Figure 4.12c and 4.12d). It is clearly seen that the charge-discharge patterns are similar to the charge-discharge pattern of pristine VA and are also consistent to their respective CV profiles. Compared to the specific capacitances derived from VA, the initial discharge and charge specific capacitances delivered from rGO/VA were 614 Fg^{-1} and 440 Fg^{-1} respectively (Figure 4.12c). Similarly, the first cycle’s discharge and charge specific capacitances of CNT/VA were 1020 Fg^{-1} and 690 Fg^{-1} respectively, which are significantly greater than the capacities achieved from rGO/VA as well as the pristine VA (Figure 4.12d). In addition, the long term cycling stability at current density of 1

Ag^{-1} over 100 cycles were found to be 65 Fg^{-1} and 71 Fg^{-1} for rGO/VA and CNT/VA respectively (Figure 4.12e). However, capacity decline still persists.

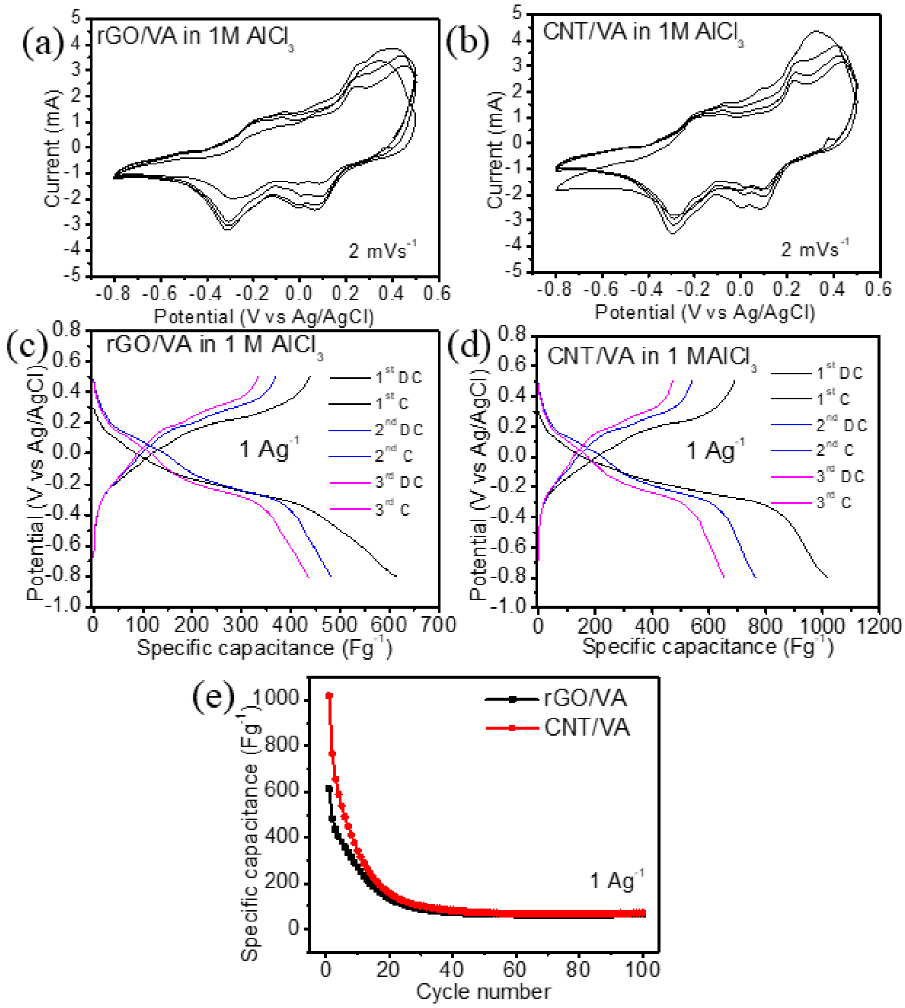

Figure 4.12: CV profiles of (a) rGO/VA and (b) CNT/VA at scan rate of 2 mVs^{-1} in 1 M $AlCl_3$, charge- discharge profiles of (c) rGO/VA and (d) CNT/VA, (e) Comparison of cycle stability at current density of 1 Ag^{-1} in 1 M $AlCl_3$ aqueous electrolyte.

Figure 4.13 shows the ex-situ XRD pattern of the VA electrode after 1st discharge and 1st charge states. It was observed that the XRD patterns of VA after 1st discharge and 1st charge states are different from the XRD pattern of pristine VA electrode. The peaks at $2\theta = 13.82\,^{o}$, $22.41\,^{o}$ and $36.03\,^{o}$ almost disappeared after 1st discharge and 1st charge states of the electrode. Morphological changes are also observed in the ex-situ FESEM of pristine VA and after 1st discharge state (Figure 4.14a and 4.14b). It was noticed the appearance of particle like structures (Figure 4.14b). All these observations indicate the possible change in one dimensional chain structure of VA after charge-discharge [2]. Moreover, the ex-situ Raman spectra

(Figure 4.15(a -d)) indicates that the characteristics Raman peaks for the pristine state of VA, located at 150 cm^{-1}, 265 cm^{-1} and 520 cm^{-1} shifted to 136 cm^{-1}, 274 cm^{-1} and 516 cm^{-1} respectively, after 1st and 20th discharge states. This shifting of the Raman peaks indicates the possible change in bond modes due to the insertion of Al^{3+} ion [2].

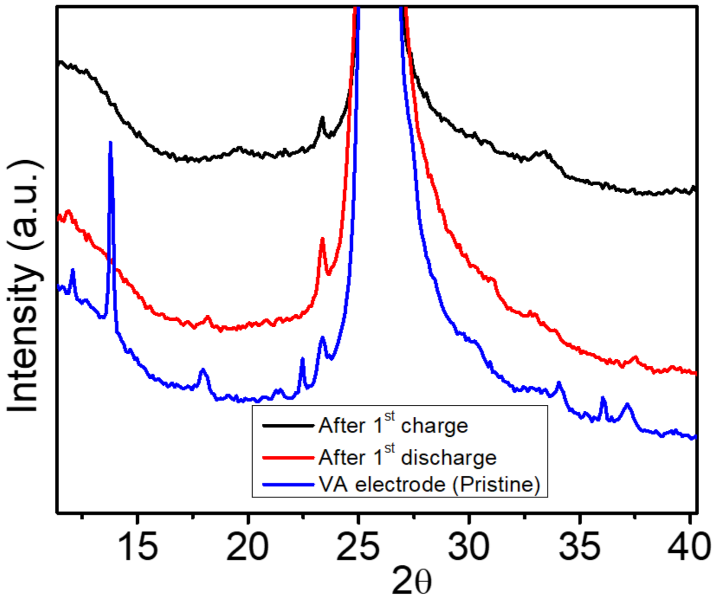

Figure 4.13: Ex-situ XRD of pristine VA electrode and after 1st charge and 1st discharge states.

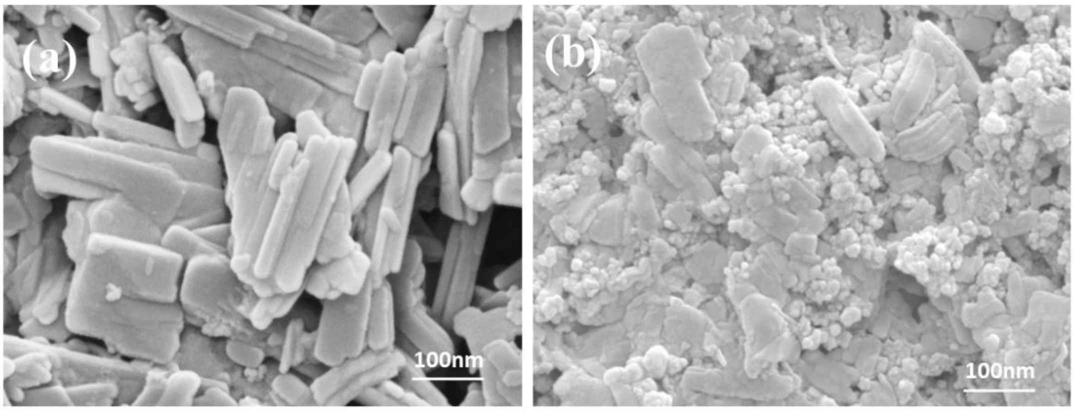

Figure 4.14: Ex-situ FESEM of (a) pristine VA electrode and (b) after 1st charge state.

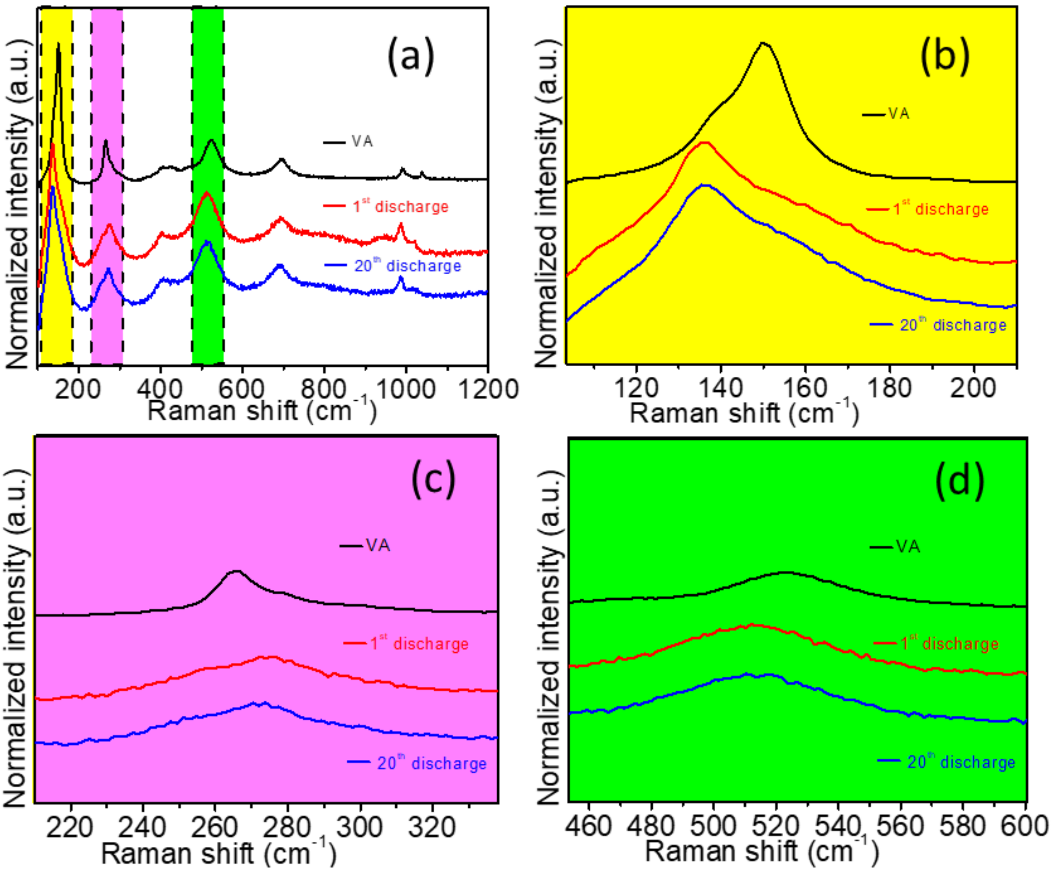

Figure 4.15: Ex-situ Raman of (a) pristine VA electrode and after 1st & 20th discharge states, enlarged view corresponding to (b) yellow, (c) pink and (d) green portions.

Furthermore, experiments were pursued to investigate the storage of Mg^{2+} and Na^{+} ions in VA. In order to study the electrochemical activity of Mg^{2+} ion, CV experiments were executed in the potential window -1 V to 0.6 V (vs Ag/AgCl) for 1 M $MgSO_4$ and 1 M $MgCl_2$ aqueous electrolytes at scan rate of 2 mVs^{-1}. In the case of 1 M $MgSO_4$ aqueous electrolyte, there exists three pairs of prominent cathodic (0.30 V, -0.25 V, -0.78 V) and anodic (0.33 V, 0.17 V, -0.13 V) peaks (Figure 4.16a). Similar trend is also seen for 1 M $MgCl_2$ aqueous electrolyte except an additional anodic peak (A) (Figure 4.16b). To calculate the Mg^{2+} ion storage capacity, charge discharge experiments were also carried out. Figure 4.16(c-d) shows the charge discharge profiles for 1 M $MgSO_4$ and 1 M $MgCl_2$ aqueous electrolytes. The broad electrochemical activities were seen in the charge discharge profiles. The discharge specific capacitances at current density of 1 Ag^{-1} for the first cycle were estimated as 308 Fg^{-1} and 550 Fg^{-1} for 1 M $MgSO_4$ and 1 M $MgCl_2$ respectively (Figure 4.16(c-d)). Now after performing the cycle stability test, it was found the specific capacitances over 100 cycles as 42 Fg^{-1} and 70 Fg^{-1} for 1 M $MgSO_4$ and 1 M $MgCl_2$ electrolytes respectively (Figure 4.16e).

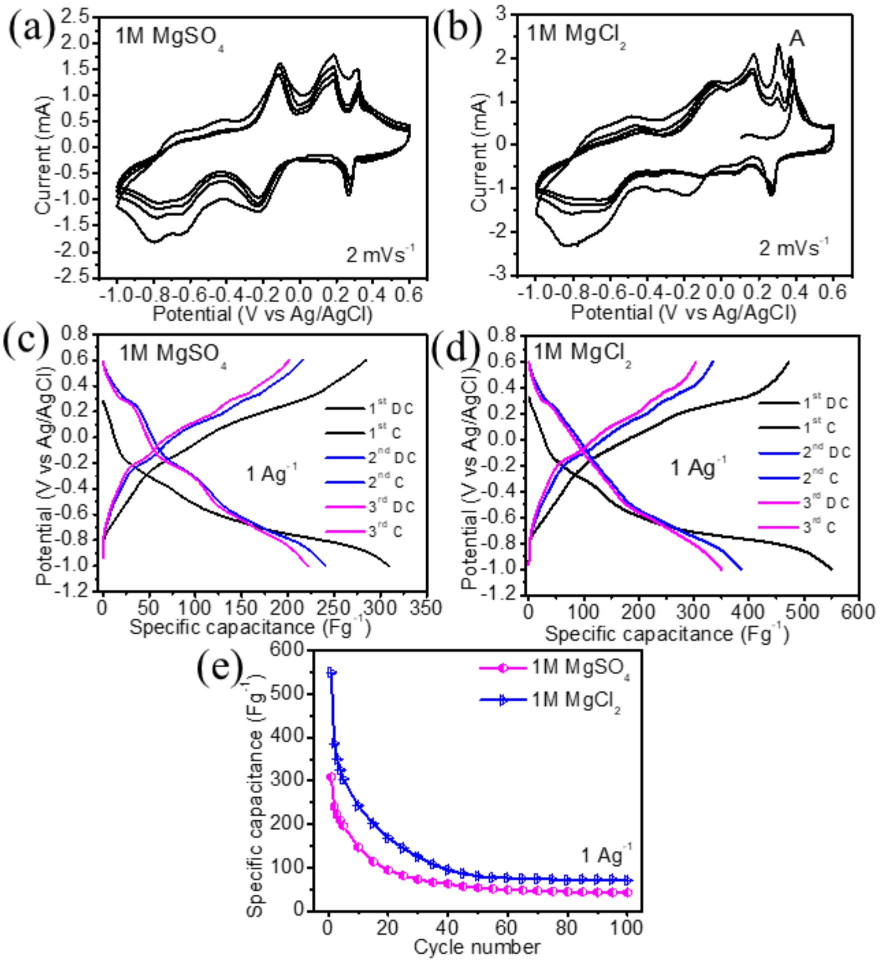

Figure 4.16: CV profiles of (a) VA in 1 M $MgSO_4$ and (b) 1 M $MgCl_2$ electrolytes at scan rate of 2 mVs^{-1}, Charge-discharge profiles of VA in (c) in 1 M $MgSO_4$ and (d) 1 M $MgCl_2$ electrolytes at current density of 1 Ag^{-1} and (e) Comparison of cycle stability at current density of 1 Ag^{-1} over 100 cycles.

Besides, in order to study the electrochemical activity of Na^+ ion, cyclic voltammetry (CV) experiments of VA were performed in 0.5 M Na_2SO_4 and 1 M NaCl aqueous electrolytes in the identical potential window (vs Ag/AgCl) at scan rate of 2 mVs^{-1} (Figure 4.17 (a-b)). For the case of 0.5 M Na_2SO_4, two sharp cathodic peaks were observed at potentials of -0.24 V and -0.38 V followed by three broad anodic peaks at -0.07 V, 0.38 V and 0.45 V (Figure 4.17a). Again, the subsequent CV profiles are superimposed indicating an electrochemical stability. Similar features were also noticed for the case of 1 M NaCl aqueous electrolyte (Figure 4.17b).

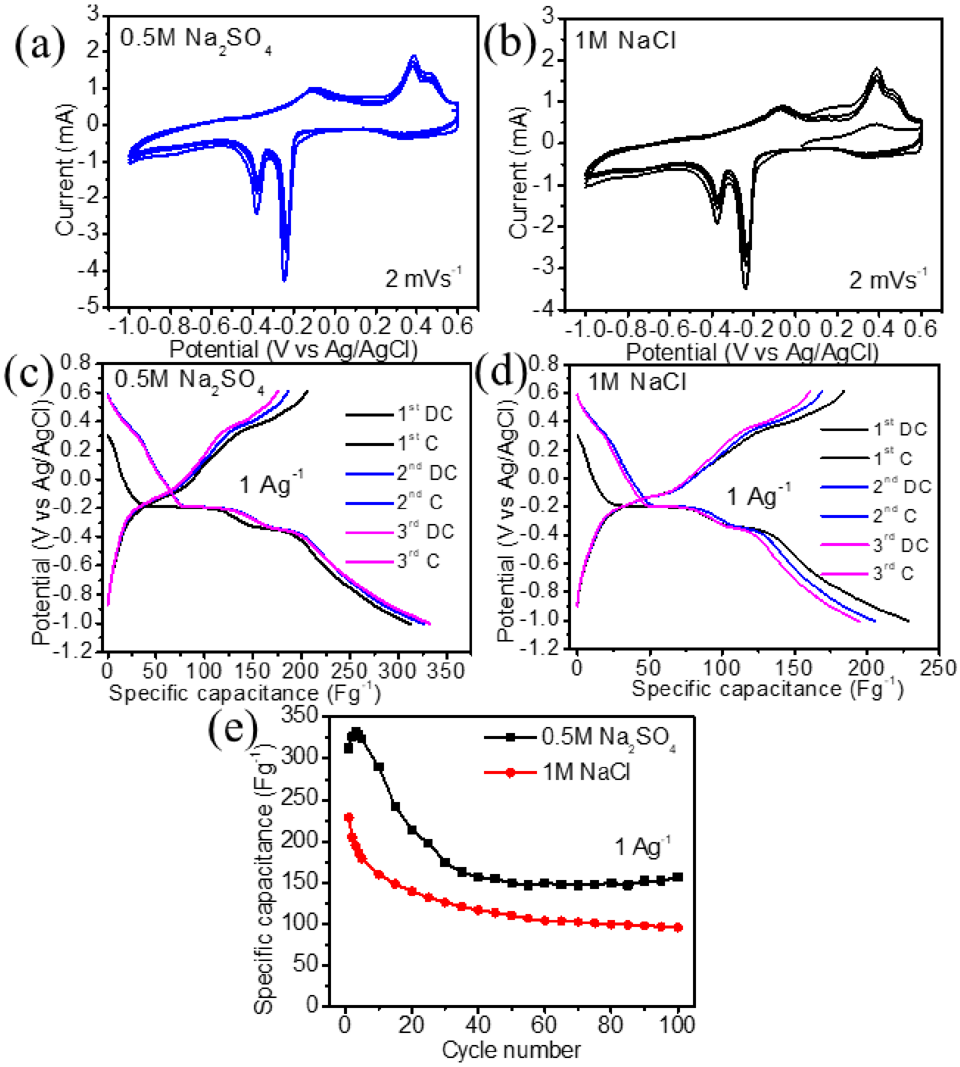

Figure 4.17: CV profiles of (a) VA in 0.5 M Na_2SO_4 and (b) 1 M NaCl electrolytes at scan rate of 2 mVs^{-1}, Charge -discharge profiles of VA in (c) in 0.5 M Na_2SO_4 and (d) 1 M NaCl electrolytes at current density of 1 Ag^{-1} and (e) Comparison of cycle stability at current density of 1 Ag^{-1} over 100 cycles.

In order to appraise the Na^+ ion storage capacity in VA, galvanostatic charge-discharge experiments were conducted in the potential window -1 V to 0.6 V for 0.5 M Na_2SO_4 and 1 M NaCl aqueous electrolytes (Figure 4.17c and 4.17d). The initial discharge specific capacitances at current density of 1 Ag^{-1} were evaluated as 229 Fg^{-1} and 312 Fg^{-1} for 0.5 M Na_2SO_4 and 1 M NaCl aqueous electrolytes respectively. Interestingly, for Na^+ ion storage investigation in VA, we could see higher cycling stable specific capacitance. The specific capacitance values of VA in 0.5 M Na_2SO_4 and 1 M NaCl electrolytes at current density of 1 Ag^{-1} over 100 cycles were calculated as 156 Fg^{-1} and 96 Fg^{-1} respectively (Figure 4.17e).

The Na⁺ ion storage in VA was further analyzed by ex-situ characterization methods. Figure 4.18 shows the EDS spectra of VA electrode after 1st discharge state. Here it is visible the peak of Na with an atomic percentage of 13.9 %, demonstrates the presence of Na^+ ion in VA (Figure 4.18 (inset table)). The elemental mappings are also shown (Figure 4.19).

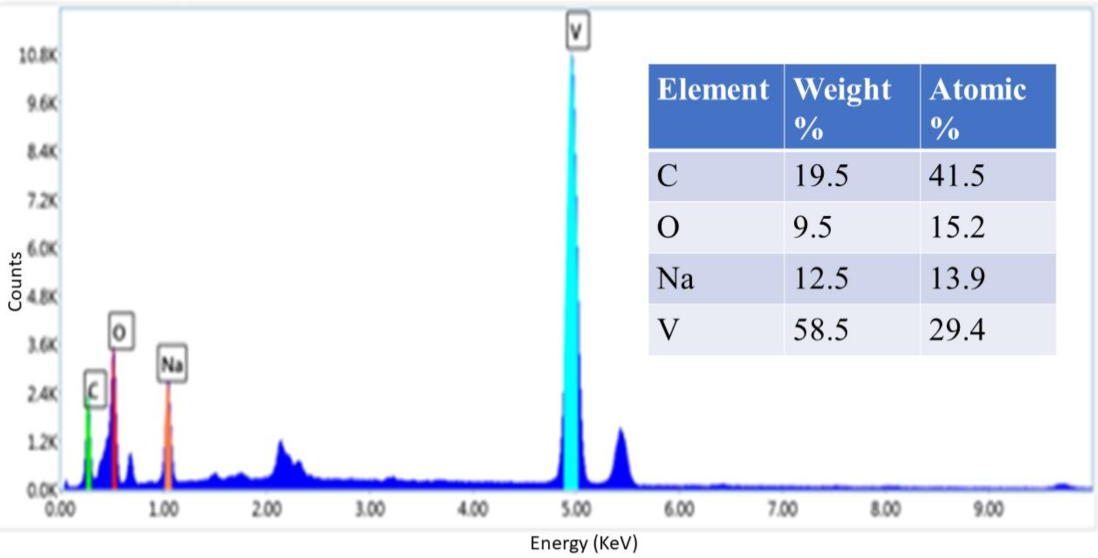

Element	Weight %	Atomic %
C	19.5	41.5
O	9.5	15.2
Na	12.5	13.9
V	58.5	29.4

Figure 4.18: EDS spectra of VA after 1st discharge state and the corresponding atomic percentages of the elements (inset table).

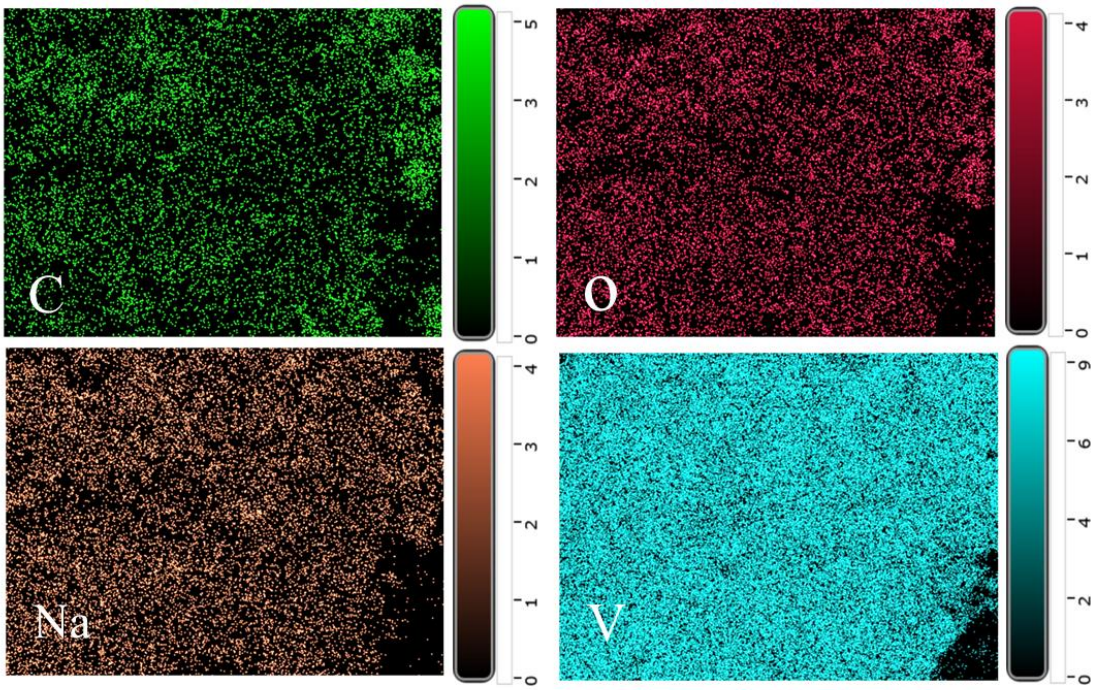

Figure 4.19: Elemental mappings of VA electrode material after 1st discharge state.

Thereafter, in order to perceive the influence in the various atomic bonds of VA after the insertion of Na^+, ex-situ Raman analysis also carried out for pristine VA electrode as well as after 1st and 20th discharge states (Figure 4.20a). All the characteristics Raman peaks are observed after the electrochemical process. However, the peak positions are slightly shifted when compared with the pristine VA electrode, which can be ascribed to the change in bonding modes on account of Na^+ ion insertion (Figure 4.20 (a-c)) [2].

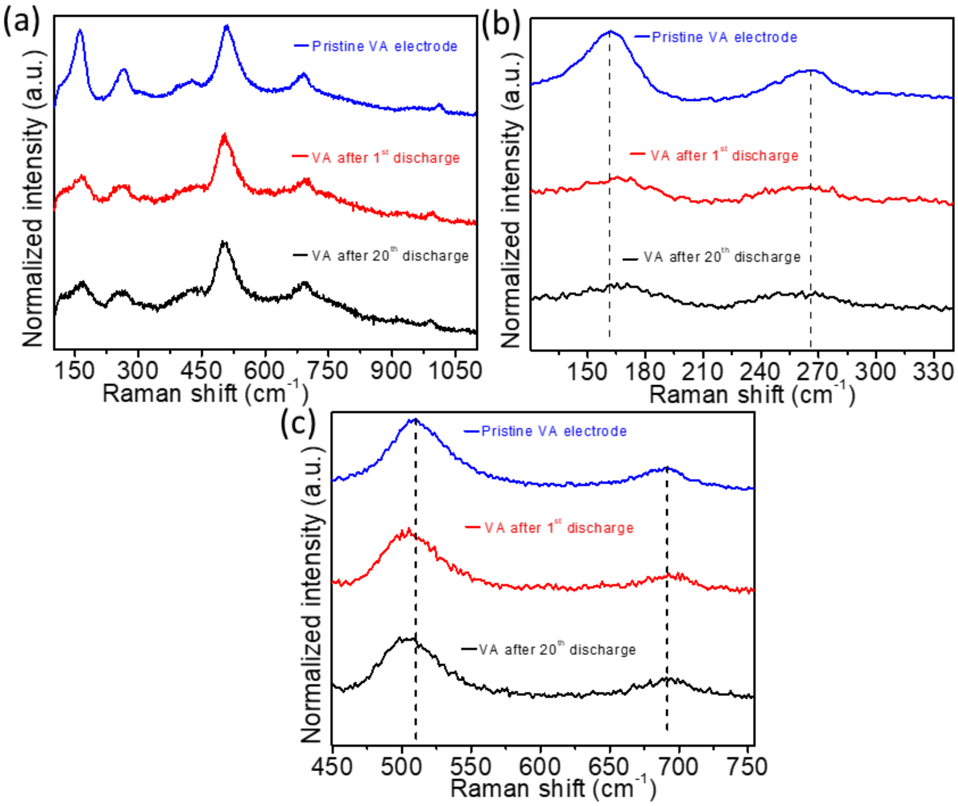

Figure 4.20: (a) Ex-situ Raman spectra of VA after 1st and 20th discharge states, (b-c) enlarged view of the peaks at 161 cm^{-1}, 263 cm^{-1}, 510 cm^{-1} and 695 cm^{-1}.

The ex-situ XRD spectra of VA after fully 1st discharged and charged cycles are displayed in (Figure 4.21a). It is seen that all the intense diffraction peaks are disappeared except two broad peaks around 2ϴ = 30° & 41° which are the characteristic peaks of carbon black used during the slurry preparation. However, the exact reasons for the disappearance of the diffraction peaks of the VA material could not be identified. We also performed the ex-situ FESEM analysis and compared to pristine VA electrode (Figure 4.21b), the ex-situ FESEM images indicate crumbling of the original structure after discharge and charge (Figure 4.21 (c-d)).

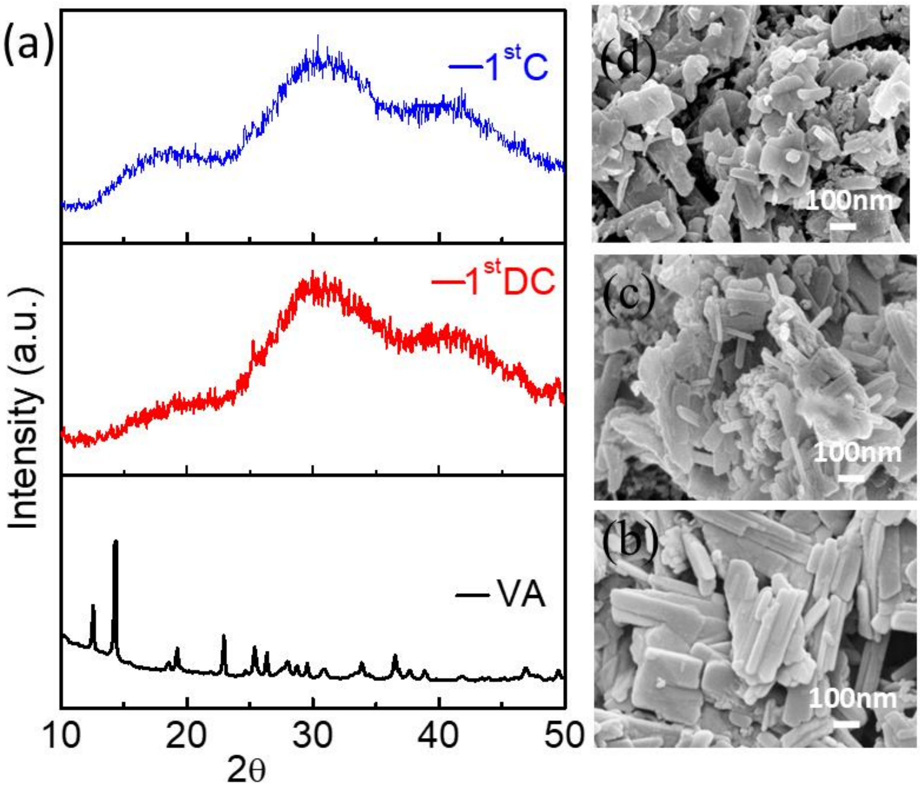

Figure 4.21: (a) Ex-situ XRD patterns of pristine VA, 1st discharged and 1st charged state electrodes, FESEM images of (b) pristine VA electrode, (c) 1st discharged state and (d) 1st charged state electrodes in 0.5 M Na_2SO_4 electrolyte.

Now in comprehensive, we compared the cycling stability of VA in 0.5 M $Al_2(SO_4)_3$, 1 M $MgSO_4$ and 0.5 M Na_2SO_4 (Figure 4.22a) at current density of 1 Ag^{-1} over 100 cycles and similarly for 1 M $AlCl_3$, 1 M $MgCl_2$ and 1 M NaCl (Figure 4.22b). The calculated stable specific capacitance values are given in the table 4.1.

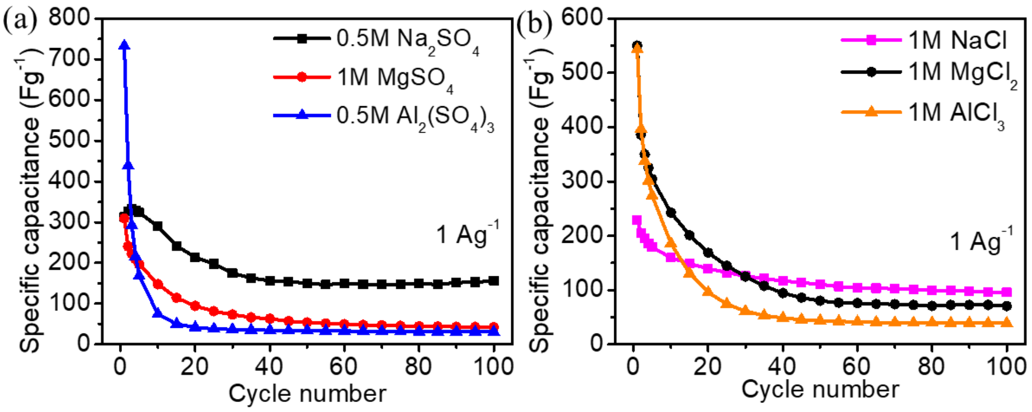

Figure 4.22: Comparison of cycling stability at current density of 1 Ag^{-1} over 100 cycles in (a) 0.5 M $Al_2(SO_4)_3$, 1 M $MgSO_4$, 0.5 M Na_2SO_4 and (b) 1 M $AlCl_3$, 1 M $MgCl_2$, 1 M NaCl electrolytes over 100 cycles.

Table 4.1: Comparison of stable specific capacitances at different electrolytes.

Electrode	Electrolyte	Stable specific capacitance over 100 cycles (Fg^{-1})
VA	0.5 M $Al_2(SO_4)_3$	30
VA	1 M $MgSO_4$	42
VA	0.5 M Na_2SO_4	156
VA	1 M $AlCl_3$	39
VA	1 M $MgCl_2$	70
VA	1 M NaCl	96

Apart from that, during the electrochemical experiments, it was noticed that the color of the electrolyte turns to greenish which may be because of the slight dissolution of VA (Figure 4.23). This can be a possible reason for the decrease in specific capacitance during the initial cycles.

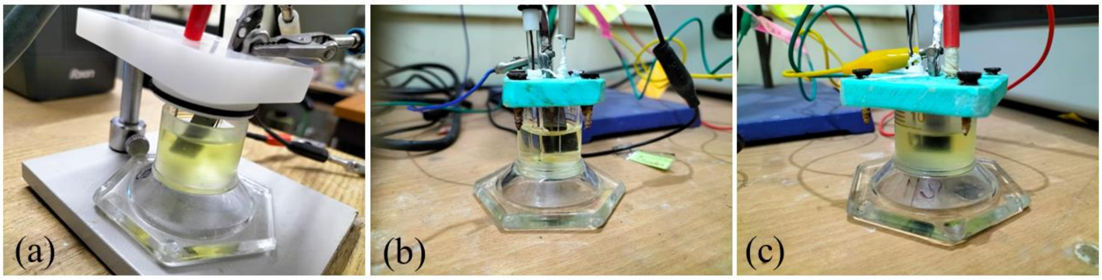

Figure 4.23: Digital Photographs of electrolytes (a) 0.5 M $Al_2(SO_4)_3$, (b) 1 M $MgSO_4$ and (c) 0.5 M Na_2SO_4 after 100 cycles.

Finally, a symmetric supercapacitor was assembled using both the electrodes as VA // VA in Na^+ ion based electrolytes only. Since the potential window is an important factor for supercapacitor [13], therefore a series of CV experiments were conducted in the potential windows ranging from (0-1.4) V to (0-2.2) V (Figure 4.24(a-e)). In the potential windows (0-1.4) V and (0-1.6) V, the CV profiles show similar behavior. But beyond (0-1.6) V, it was observed that the current response sharply increases in higher potential as well as the peak current response decreases (Figure 4.24 (c-e)). That is why, we optimized the potential window as (0-1.6) V for 0.5 M Na_2SO_4 (aq) electrolyte. As shown in (Figure 4.24b), the intense cathodic peak was recognized at 0.85 V and two broad cathodic peaks were marked at 1.2 V and 0.4

V. On the other hand, two prominent anodic peaks were noticed at 0.83 V and 1.2 V. However, no noticeable peak was observed for bare graphite // bare graphite electrode within the same potential window (Figure 4.25).

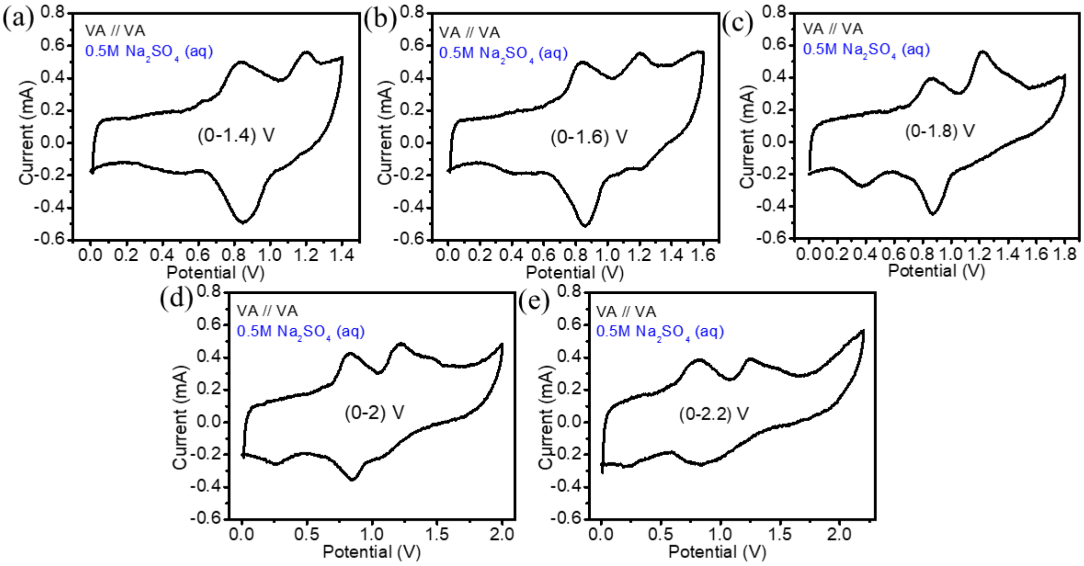

Figure 4.24: CV curves of VA // VA symmetric supercapacitor at scan rate of 2 mVs^{-1} in 0.5 M Na_2SO_4 (aq) electrolyte for the potential window (a) (0-1.4) V, (b) (0-1.6) V, (c) (0-1.8) V, (a) (0-2) V and (e) (0-2.2) V.

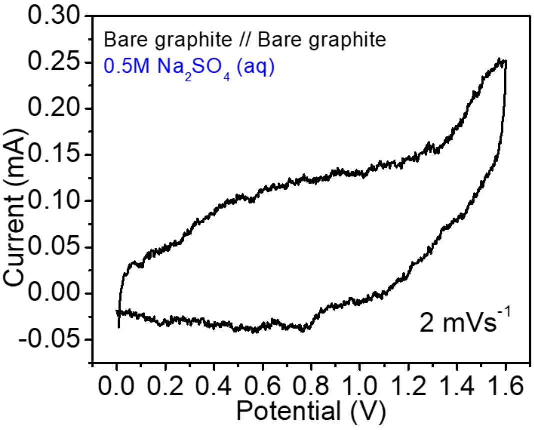

Figure 4.25: CV profile of Bare graphite // Bare graphite cell in 0.5 M Na_2SO_4 (aq) electrolyte.

Similarly, series of CV experiments were performed for 0.5 M Na_2SO_4/Gum (gel) and 0.5 M Na_2SO_4/Silica (gel) electrolytes from (0-1.6) V to (0-2.2) V at scan rate of 2 mVs^{-1} (Figure 4.26 (a-d) and 4.27 (a-d)). The CV curves in both the gel electrolytes are identical to aqueous electrolyte except one additional anodic peak at 1.5 V (Figure 4.26b & 4.27b). The current response in the CV curves after (0-1.8) V seems to increase sharply in the higher potential side, which may be due to the possible side reactions [14]. Therefore, the potential window for both the gel electrolytes are optimized as (0-1.8) V.

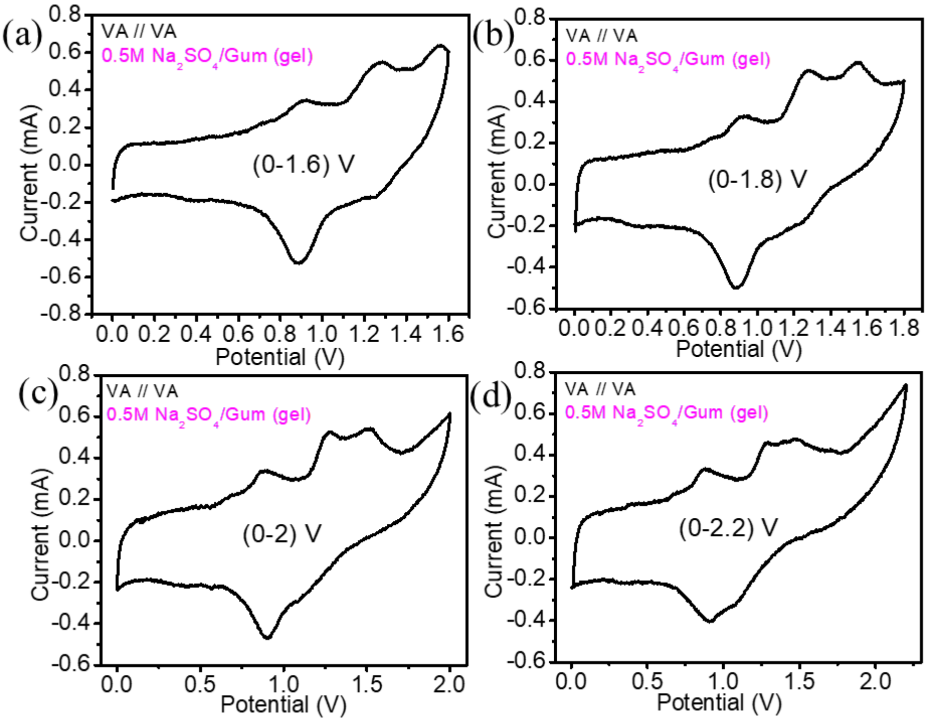

Figure 4.26: CV profiles of VA // VA cell in the potential window (a) (0-1.6) V, (b) (0-1.8) V, (c) (0-2) V, (d) (0-2.2) V in 0.5 M Na_2SO_4/Gum (gel) electrolyte.

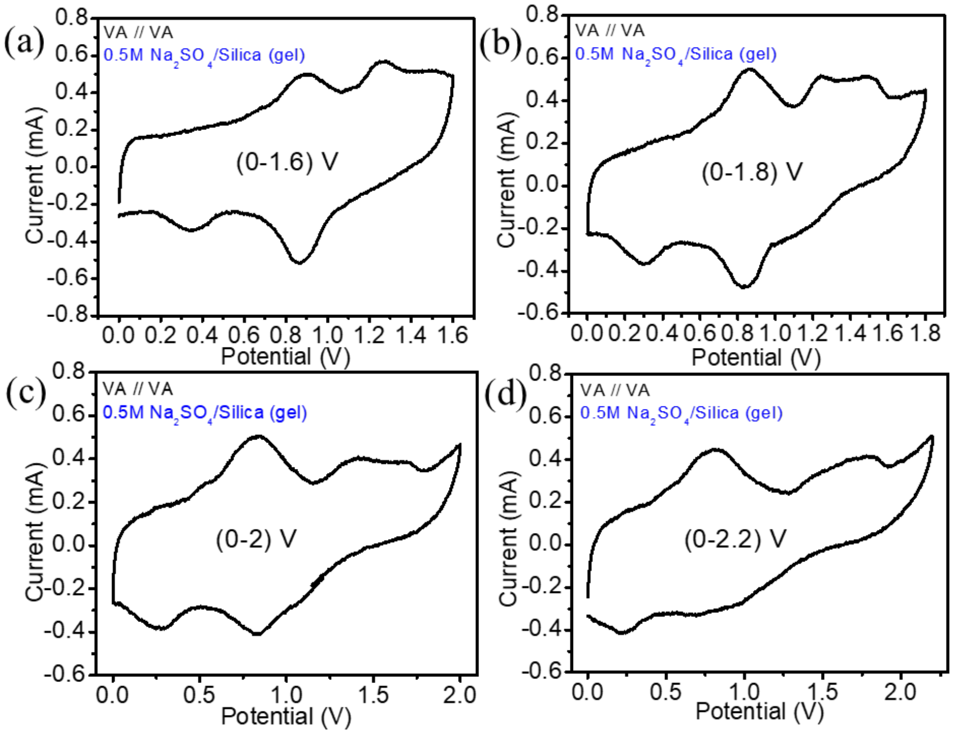

Figure 4.27: CV profiles of VA // VA cell in the potential window (a) (0-1.6) V, (b) (0-1.8) V, (c) (0-2) V, (d) (0-2.2) V in 0.5 M Na_2SO_4/Silica (gel) electrolyte.

Figure 4.28 (a-c) shows the galvanostatic charge discharge profiles of VA // VA symmetric supercapacitor in 0.5 M Na_2SO_4 (aq), 0.5 M Na_2SO_4/Gum (gel) and 0.5 M Na_2SO_4/Silica (gel) electrolytes. It was observed that the cell in these electrolytes show similar storage behavior. The initial discharge specific capacitances at current density of 0.1 Ag^{-1} were calculated to be 284 Fg^{-1}, 297 Fg^{-1} and 347 Fg^{-1} for 0.5 M Na_2SO_4 (aq), 0.5 M Na_2SO_4/Gum (gel) and 0.5 M Na_2SO_4/Silica (gel) electrolytes respectively (Figure 4.28 (a-c)). Figure 4.29 shows the rate capabilities of VA // VA cells in aqueous and gel electrolytes as a function of cycle number. The specific capacitance values for the 5th cycle of each current density in aqueous as well as gel electrolytes are listed in the table 4.2.

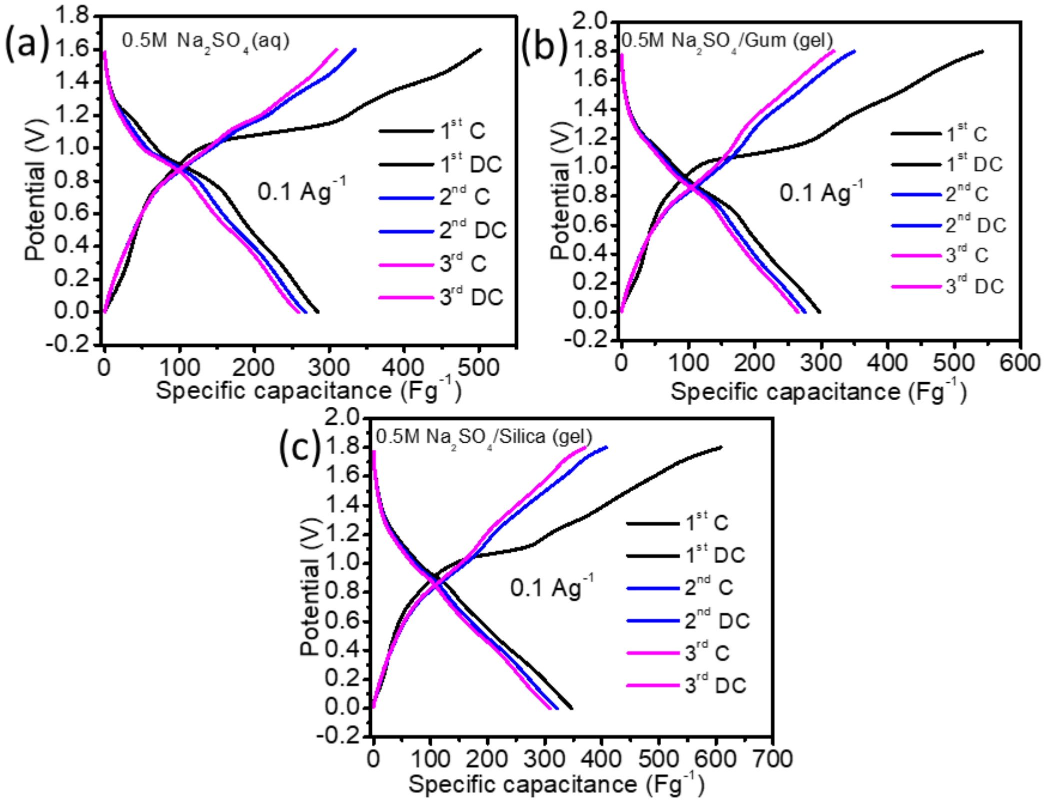

Figure 4.28: GDC profiles of VA // VA symmetric supercapacitor at current density of 0.1 Ag^{-1} in (a) 0.5 M Na_2SO_4 (aq), (b) 0.5 M Na_2SO_4/Gum (gel) and (c) 0.5 M Na_2SO_4/Silica (gel) electrolytes.

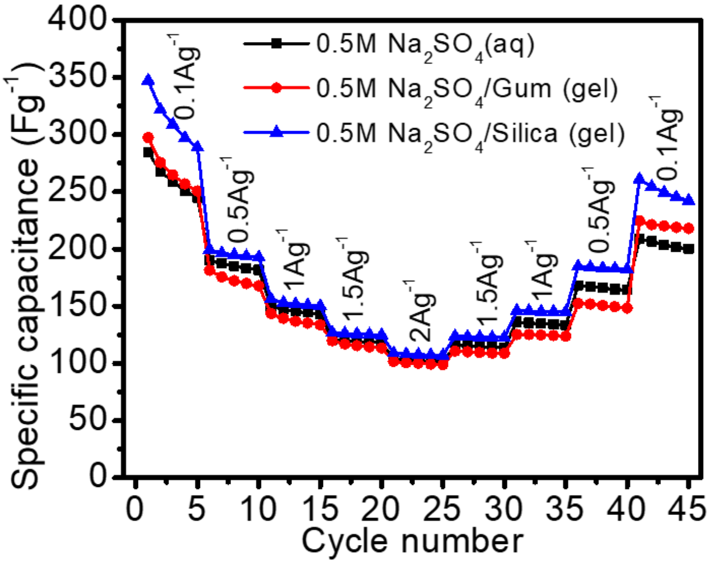

Figure 4.29: Rate capabilities of VA // VA symmetric supercapacitor in aqueous and gel electrolytes.

Table 4.2. Specific capacitance of VA // VA cells at different current densities in aqueous and gel electrolytes.

Current density (Ag^{-1})	Specific capacitance of VA // VA cell for the 5th cycle in 0.5 M Na_2SO_4 (aq) electrolyte (Fg^{-1})	Specific capacitance of VA // VA cell for the 5th cycle in 0.5 M Na_2SO_4/Gum (gel) electrolyte (Fg^{-1})	Specific capacitance of VA // VA cell for the 5th cycle in 0.5 M Na_2SO_4/Silica (gel) electrolyte (Fg^{-1})
0.1	245	250	288
0.5	182	168	193
1	143	134	150
1.5	118	113	125
2	102	99	107

It has been observed that the specific capacitance decreases with the increase of current density. The specific capacitance is more in case of lower current density (0.1 Ag^{-1}), which may be on account of full access of pores in the electrode material or more electrolytic ions can interact with the electrode material [15]. Figure 4.30a shows the comparison of energy density with power density at different current densities (i.e. 0.1 Ag^{-1}, 0.5 Ag^{-1}, 1 Ag^{-1}, 1.5 Ag^{-1} and 2 Ag^{-1}) for the used aqueous and gel electrolytes. The energy density and power density were calculated for the 5th cycle of each current density. The maximum energy density / power density delivered by VA // VA cell in 0.5 M Na_2SO_4 (aq) electrolyte was estimated about 87 Wh kg^{-1} / 80 W kg^{-1} at current density of 0.1 Ag^{-1}. While for 0.5 M Na_2SO_4/Gum (gel) and 0.5 M Na_2SO_4/Silica (gel) electrolytes, the energy density / power density was found as 113 Wh kg^{-1} / 90 W kg^{-1} and 130 Wh kg^{-1} / 90 W kg^{-1} respectively corresponding to the similar current density 0.1 Ag^{-1}. At higher current density (= 2 Ag^{-1}), the energy density / power density reaches to 36 Wh kg^{-1} / 1600 W kg^{-1}, 44 Wh kg^{-1} / 1800 W kg^{-1} and 48 Wh kg^{-1} / 1800 W kg^{-1} for 0.5 M Na_2SO_4 (aq), 0.5 M Na_2SO_4/Gum (gel) and 0.5 M Na_2SO_4/Silica (gel) electrolytes respectively. Figure 4.30b shows the long term cycling stability of VA // VA cells up to 2000 cycles in the aqueous and gel electrolytes. It was found that, the specific capacitance values at current density of 2 Ag^{-1} at 2000th cycle were 45 Fg^{-1}, 17 Fg^{-1} and 60 Fg^{-1} for 0.5 M Na_2SO_4 (aq), 0.5 M Na_2SO_4/Gum (gel) and 0.5 M Na_2SO_4/Silica (gel) electrolytes respectively.

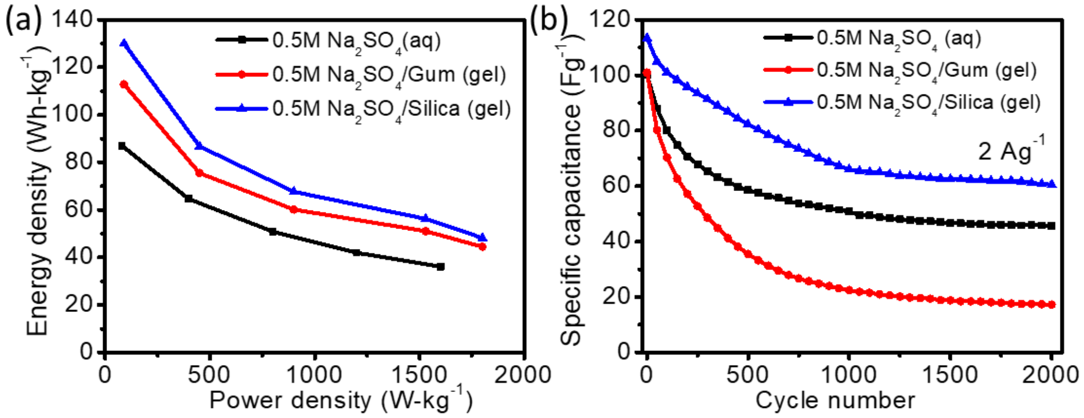

Figure 4.30: Comparisons of (a) energy densities vs power densities and (b) long term cycling stabilities (at higher current density 2 Ag^{-1} up to 2000 cycles) of VA // VA symmetric supercapacitor in aqueous as well as gel electrolytes.

4.4 Conclusion

In summary, vanadyl acetate was obtained hydrothermally and it showed the ability to store Na^+, Mg^{2+} and Al^{3+} ions. However, there is severe capacity decline for Mg^{2+} and Al^{3+} ions. There is an initial capacity decline for Na^+ ion but vanadyl acetate retains stable capacity of approximately 150 Fg^{-1} after 40 cycles at current rate of 1 Ag^{-1}. The symmetric electrochemical capacitor also shows stable specific capacity of 60 Fg^{-1} at current rate of 2 Ag^{-1}. It is noted that silica based gel electrolyte improved the performance of the capacitor. This study uniquely illustrates the importance of mono or polyvalent ions in determining the electrochemical performance of an electrochemical capacitor.

4.5 References

[1] Weeks, C., Song, Y., Suzuki, M., Chernova, N. A., Zavalij, P. Y., and Whittingham, M. S. The one dimensional chain structures of vanadyl glycolate and vanadyl acetate. *J. Mater. Chem.*, 13: 1420, 2003.

[2] Nandi, S., Yan, Y., Yuan, X., Wang, C., He, X., Li, Y., and Das, S. K. Vanadyl ethylene glycolate: A novel organic-inorganic electrode material for rechargeable aqueous aluminum-ion battery. *Solid State Ionics,* 389: 116085, 2023.

[3] Wen, N., Chen, S., Li, X., Zhang, K., Feng, J., Zhou, Z., Fan, Q., Kuang, Q., Dong, Y., and Zhao, Y. Facile synthesis of one dimensional vanadyl acetate nanobelts toward a novel anode for lithium storage. *Delton Trans*., 50: 11568, 2021.

[4] Li, Y., Zhao, Y., Wen, N., Zhou, H., Kuang, Q., Fan, Q., and Dong, Y. Solvothermal synthesis of organic inorganic cathode vanadyl acetate nanobelts for aqueous zinc-ion batteries. *ACS Sustainable Chem. Eng.*, 11: 5105, 2023.

[5] Zhou, K., Zhou, W., Liu, X., Sang, Y., Ji, S., Li, W., Lu, J., Li, L., Niu, W., Liu, H., and Chen, S. Ultrathin MoO3 nanocrystals self assembled on graphene nanosheets via oxygen bonding as supercapacitor electrodes of high capacitance and long cycle life. *Nano Energy,* 12: 510, 2015.

[6] Xiang, C., Li, M., Zhi, M., Manivannan, A., and Wu, N. Reduced graphene oxide/titanium dioxide composites for supercapacitor electrodes: shape and coupling effects, *J. Mater. Chem.,* 22: 19161, 2012

[7] Bin, D., Huo, W., Yuan, Y., Huang, J., Liu, Y., Zhang, Y., Dong, F., Wang, Y., and Xia, Y. Organic-inorganic-induced polymer intercalation into layered composites for aqueous zinc-ion battery. *Chem.*, 6: 968, 2020.

[8] Wei, T., Li, Q., Yang, S., and Wang, C. Highly reversible and long-life cycling aqueous zinc-ion battery based on ultrathin $(NH_4)_2V_{10}O_{25}\cdot 8H_2O$ nanobelts**.** *J. Mater. Chem. A*, 6: 20402, 2018.

[9] . Kumar, S., Satish R., Verma, V., Ren, H., Kidkhunthod, P., Manalastas, Jr., and Srinivasan, M. Investigating $FeVO_4$ as a cathode material for aqueous aluminum-ion battery. *J. Power sources,* 426: 151, 2019.

[10] Rahman, A., Sarmah, D., and Das, S. K. A study on Al^{3+} ion capacitor with MoO_3 nanorod and aqueous gel electrolyte. *Ionics,* 29: 4253, 2023.

[11] Tran, D. T., and Nguyen, V. N. rGO/persulphate metal free catalytic system for the degradation of tetracycline: effect of reaction parameters. *Mater. Res. Express*. 7: 075501, 2020.

[12] Jorio, A., and Saito, R. Raman spectroscopy for carbon nanotube applications. *J. Appl. Phys.,* 129: 021102, 2021.

[13] Gogotsi, Y., and Penner, R. M. Energy Storage in Nanomaterials - capacitive, pseudocapacitive, or battery-like? *ACS Nano,* 12: 2081, 2018.

[14] Sarmah, D. and Kumar, Ashok. Symmetric supercapacitors with layer-by-layer molybdenum disulfide reduced graphene oxide structures and poly(3,4-ethylenedioxythiophene) nanoparticles nanohybrid electrode. *J. Energy Storage,* 35:102289, 2021.

[15] Kubra, K. T., Sharifa, R., Patil, B., Javaid, A., Shahzadi, S., Salman, A., Siddique, S., and Ali, G. Hydrothermal synthesis of neodymium oxide nanoparticles and its nanocomposites with manganese oxide as electrode materials for supercapacitor application. *J. Alloys Compd.,* 815: 152104, 2020.